

Visible-to-near-infrared octave spanning supercontinuum generation in a silicon nitride waveguide

Haolan Zhao,^{1,2,*} Bart Kuyken,^{1,2} Stéphane Clemmen,^{1,2} François Leo,^{1,2} Ananth Subramanian,^{1,2} Ashim Dhakal,^{1,2} Philippe Helin,³ Simone Severi,³ Edouard Brainis,^{2,4} Gunther Roelkens,^{1,2} and Roel Baets^{1,2}

¹Photonics Research Group, Department of Information Technology, Ghent University-imec, Sint-Pietersnieuwstraat 41, 9000 Ghent, Belgium

²Center for Nano- and Biophotonics (NB-Photonics), Ghent University, Sint-Pietersnieuwstraat 41, 9000 Ghent, Belgium

³imec, Kapeldreef 75, B-3001 Leuven, Belgium

⁴Physics and Chemistry of Nanostructures Group, Ghent University, Krijgslaan 281-S3, 9000 Ghent, Belgium

*Corresponding author: haolan.zhao@ugent.be

Received February 25, 2015; revised April 10, 2015; accepted April 10, 2015;
posted April 17, 2015 (Doc. ID 234835); published May 4, 2015

The generation of an octave spanning supercontinuum covering 488–978 nm (at –30 dB) is demonstrated for the first time on-chip. This result is achieved by dispersion engineering a 1-cm-long Si₃N₄ waveguide and pumping it with an 100-fs Ti:Sapphire laser emitting at 795 nm. This work offers a bright broadband source for biophotonic applications and frequency metrology. © 2015 Optical Society of America

OCIS codes: (320.6629) Supercontinuum generation; (190.4390) Nonlinear optics, integrated optics.

<http://dx.doi.org/10.1364/OL.40.002177>

Over the last decade, the progress of supercontinuum (SC) generation in photonic crystal fibers [1–3] has led to a series of advancements in spectroscopy [4], optical coherence tomography [5], and precise frequency metrology [6]. Recently SC generation on integrated CMOS-compatible waveguide platforms has been attracting significant attention. Previous efforts mostly aimed at the telecom wavelength window [7] for WDM communication and at the mid-infrared range [8] for spectroscopic sensing. However, a SC covering the red to near-infrared spectral window where tissue and cells possess low absorption and scattering coefficients could offer particular advantages for biological applications such as bioimaging [9] and Raman spectroscopy [10,11].

To produce a SC below 1 μm on a CMOS-compatible integrated platform, there are two main hurdles to overcome: transparency of the waveguide and phase matching. The first one can be addressed by using silicon nitride as the waveguide material rather than silicon [12]. Recently, a SC down to 665 nm has been obtained using a silicon nitride waveguide pumped at 1335 nm [13]. The second hurdle is to obtain anomalous dispersion required for efficient SC generation in Si₃N₄ waveguides. At visible wavelengths, this is not trivial because Si₃N₄ possesses a strong normal material dispersion due to the proximity to the material bandgap. The strong normal material dispersion thus needs to be compensated by the waveguide dispersion. A frequency comb using a silicon nitride microcavity has been demonstrated with comb lines down to 765 nm circumventing this requirement by using a combination of $\chi^{(2)}$ and $\chi^{(3)}$ nonlinear processes [14], yet it requires careful dispersion management. In this report, inspired by the work on silicon platform [15,16], we implement a similar method to achieve anomalous dispersion in a silicon nitride waveguide by partially underetching the silicon oxide underneath the Si₃N₄ waveguide core. We demonstrate an SC ranging from 488 to 978 nm when pumping the waveguide at 795 nm. To the best of our knowledge, this is the first demonstration of an octave-spanning supercontinuum extending in the sub-500-nm wavelength range on an

integrated platform. It constitutes a first step to a fully integrated broadband source for, e.g., biophotonic applications.

The waveguide used in the experiment is fabricated in a CMOS pilot line at imec [17]. A 300-nm-thick silicon nitride film is grown via low-pressure chemical vapor deposition (LPCVD) on a 1.6-μm buried silicon oxide layer (BOX). A 500-nm-wide waveguide of 1 cm length is then defined in the thin film using deep UV lithography and dry etching. The air-clad waveguide is then dipped into diluted HF, which partially etches the oxide underneath it. Given the high etching selectivity between SiO₂ and LPCVD Si₃N₄ (200:1), the Si₃N₄ waveguide dimensions are quasi-conserved. A schematic cross-section of the waveguide is shown in Fig. 1(a) while an SEM picture is shown in Fig. 1(b). The waveguide propagation loss after underetching is measured with a commercial supercontinuum source (NKT superK EXR-4) in a cutback measurement and the result is shown in Fig. 1(c). The waveguide loss from 650 to 850 nm is about

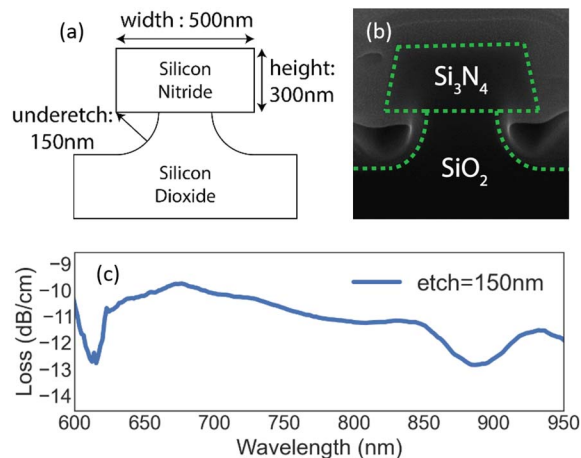


Fig. 1. (a) Schematic cross-section of the waveguide. (b) SEM picture of the waveguide cross-section. The material around the silicon nitride core is deposited for FIB cross-section. (c) The waveguide propagation loss from 600 to 950 nm.

11 dB/cm. The increased index-contrast that is obtained by removing the oxide allows for increased confinement and hence stronger waveguide dispersion, compensating for the strong material dispersion of silicon nitride at visible wavelengths. Taking into account the material dispersion, the dependence of group velocity dispersion (GVD) on wavelength for the fundamental quasi-TE mode of the engineered waveguide is obtained via a full vectorial mode solver and the result is shown in Fig. 2. We can readily observe that an increase in the underetching results in an increased anomalous GVD. The waveguide we design for SC generation has an etching depth of 150 nm, carrying an anomalous dispersion between 740 and 907 nm, and the GVD of final waveguide lies in the shaded area due to fabrication uncertainty. The increased confinement also enhances the nonlinearity of the waveguide by reducing the mode area such that we obtain an effective nonlinearity of $7 \text{ W}^{-1} \text{ m}^{-1}$ at 795 nm by assuming a nonlinear index $n_2 = 24 \times 10^{-20} \text{ m}^2/\text{W}$ [18].

Figure 3 shows the schematic experimental setup for SC generation. We use a pulse train generated by a Ti:Sapphire laser (Mai Tai, Spectra-Physics) operating at 795 nm as a pump. The pulses have a nominal squared hyperbolic secant shape in the temporal domain with a FWHM of 100 fs and a repetition rate of 80 MHz. To ensure the excitation of the fundamental TE mode in waveguide, a combination of a half-wave plate and a polarizing beam splitter is used. The pump is coupled into the waveguide using a microscope objective (40 \times , NA = 0.5), and the generated spectrum is coupled out using a lensed fiber (NA = 0.2). The coupling loss at the input is measured to be 8.5 dB.

We use an optical spectrum analyzer (450–1050 nm, Advantest Q8381A) to record the generated spectrum. Figure 4 shows the measured spectra at various input peak powers coupled into the waveguide. At a low peak power of 62 W, the spectral width is the same as the input pulse. At 182 W, small ripples emerge in the center of the pulse, which is attributed to self-phase modulation (SPM). At 491 W, we see clearly two peaks emerging at 917 and 495 nm. Since the peaks appear at a wavelength where the waveguide has normal dispersion, we attribute these two peaks to dispersive waves. When the power is further increased, the dispersive wave centered at

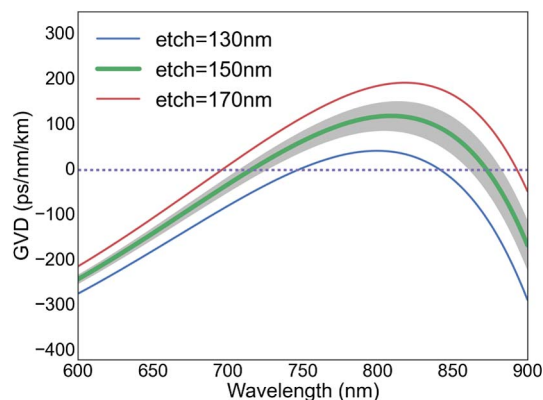


Fig. 2. Group velocity dispersion (GVD) of the underetched Si_3N_4 waveguide for various values of the waveguide underetching. The GVD of waveguide used in the experiment lies in the shaded area.

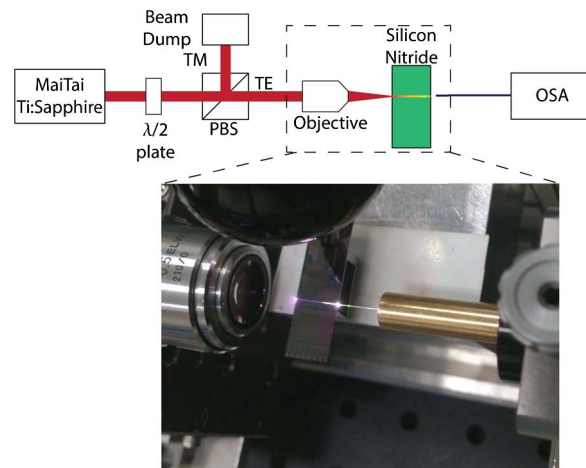


Fig. 3. Setup of the experiment. Visible light generation from the end of the chip can readily be observed.

917 nm red-shifts to 937 nm, while the one at 495 nm retains its original spectral position. At the maximal available coupled power of 874 W, the -30 dB bandwidth spans 490 nm from 488 to 978 nm, slightly more than an octave. From Fig. 3, one can clearly see visible red light generated right after the input, and its intensity increasing along the propagation direction. Further increasing the power would help improve the spectral homogeneity, yet the limitation is the damage occurring at the input facet of the waveguide. To ensure no spectral broadening takes place in the collection fiber, we deliberately misaligned the lensed fiber both vertically and horizontally at the output facet to reduce the spectrum recorded in OSA by 20 dB at the same coupling angle, and we observe no change in the shape of the spectrum.

To gain insight in the physical mechanism behind the spectral broadening, we model the SC generation in our waveguide with the Nonlinear Schrödinger Equation (NLSE). This equation describes the evolution of the temporal envelop of the electric field $E(z, t)$ inside the nonlinear medium, taking into account the propagation loss, SPM, GVD, and self-steepening effects. The equation reads [1]:

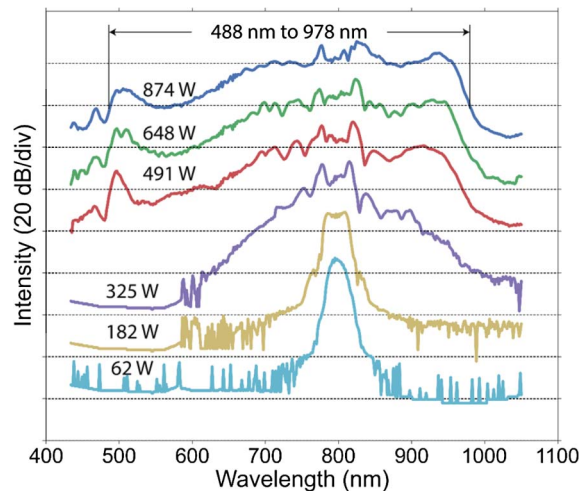


Fig. 4. Output spectra of the waveguide at various input peak power coupled into the waveguide. The spectra are shifted vertically for clarity.

$$\frac{\partial E(z, t)}{\partial z} = i \sum_{k \geq 2} i^k \frac{\beta_k}{k!} \frac{\partial^k E}{\partial t^k} - \frac{\alpha_l}{2} E + i\gamma \left(|E|^2 E + \frac{i}{\omega_p} \frac{\partial}{\partial t} (|E|^2 E) \right). \quad (1)$$

Here β_k is the k -th order chromatic dispersion obtained by Taylor series expansion of the wave number β , α_l is the linear loss of the waveguide, ω_0 is the pump frequency, and γ is the nonlinear coefficient of the waveguide. The Raman term is omitted in the equation since its contribution is rather limited [19,20].

The NLSE is numerically solved with the split-step Fourier algorithm using the chromatic dispersion up to the 6th order, and we have to plug in the spectral dependence of mode area into calculation. Figure 5 shows the evolution of the pulse inside the waveguide. Because the waveguide dimensions determined by SEM picture involve a certain degree of uncertainty (~ 15 nm), the dispersions are determined by fitting the experimental data with boundary conditions as shown in the shaded area in Fig. 2. The top panel plots the output pulse spectrum of both the simulation and the measurement, which reveals a reasonable agreement in terms of the general shape. The spectral width and the positions of the two dispersive waves in the experiment are reproduced by the simulation. The simulation accounts for a slight chirp of the input pulse of 0.15 extracted by fitting output spectrum at 182 W. It is noticeable that the predicted peak power at 495 nm is around 8 dB higher than the measurement, which we attribute to a combination of higher scattering loss and stronger material absorption at shorter wavelength. The increased loss is reflected in a measurement with 445 nm laser (Wicked Laser, Spyder 3) where we found the waveguide becomes so lossy that no light could transmit through.

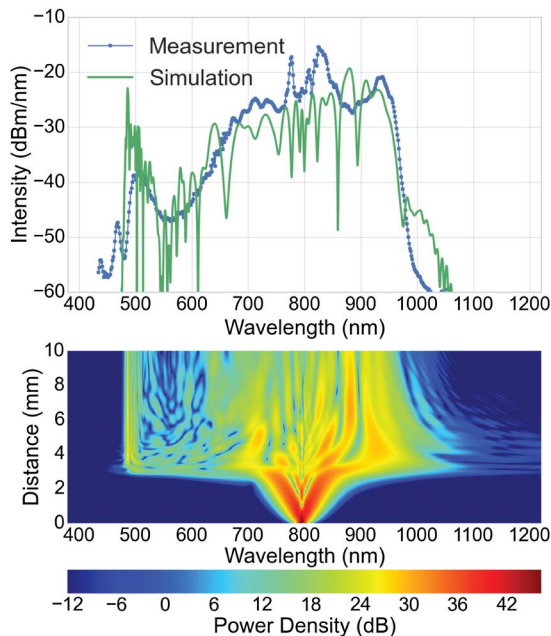


Fig. 5. (Top) Comparison between measured spectrum and simulation in the output and (below) evolution of the pulse inside waveguide with 874-W input peak power.

The position of the dispersive waves can also be predicted by the phase-matching condition [1]:

$$\beta(\omega_{\text{DW}}) - \frac{\omega_{\text{DW}}}{v_{g,s}} = \beta(\omega_s) - \frac{\omega_s}{v_{g,s}} + \frac{\gamma P_s}{2}. \quad (2)$$

Here β is the wave number, γ is the nonlinear coefficient, $v_{g,s}$ is the soliton group velocity, P_s is the soliton peak power, and ω_{DW} and ω_s are the frequency of dispersive wave and soliton, respectively. By using a peak soliton power of 874 W, the dispersive waves are predicted to appear at 934 and 498 nm, which is in agreement with the experiment. The deviations between simulation and measurement are attributed to uncertainty of waveguide dimensions. With the phase-matching condition, the redshift of the near-infrared dispersive wave can be readily explained by the variation in soliton power. We believe the calculation based on the phase-matching condition and the numerical simulation results confirm the origin of the peaks.

In conclusion, we have demonstrated an octave-spanning SC covering a large part of the visible spectrum in a partially underetched dispersion engineered silicon nitride waveguide. To the best of our knowledge, this work constitutes the first visible SC on an integrated platform, offering a novel, compact, visible broadband source for Raman spectroscopy, confocal microscopy, optical coherence tomography, and precise frequency metrology. Our result also shows one can tailor the zero dispersion wavelength to the visible wavelength region in the Si_3N_4 platform, offering further opportunities for nonlinear optics at visible wavelengths.

The work is supported by the FP7-ERC-InSpectra advanced grant.

References

1. J. M. Dudley, G. Genty, and S. Coen, *Rev. Mod. Phys.* **78**, 1135 (2006).
2. C. R. Petersen, U. Mller, I. Kubat, B. Zhou, S. Dupont, J. Ramsay, T. Benson, S. Sujecki, N. Abdel-Moneim, Z. Tang, D. Furniss, A. Seddon, and O. Bang, *Nat. Photonics* **8**, 830 (2014).
3. M.-T. Tsai and M.-C. Chan, *Opt. Lett.* **39**, 865 (2014).
4. K. Lindfors, T. Kalkbrenner, P. Stoller, and V. Sandoghdar, *Phys. Rev. Lett.* **93**, 037401 (2004).
5. R. Leitgeb, W. Drexler, A. Unterhuber, B. Hermann, T. Bajraszewski, T. Le, A. Stingl, and A. Fercher, *Opt. Express* **12**, 2156 (2004).
6. T. Udem, R. Holzwarth, and T. W. Hänsch, *Nature* **416**, 233 (2002).
7. J. Safioui, F. Leo, B. Kuyken, S.-P. Gorza, S. K. Selvaraja, R. Baets, P. Emplit, G. Roelkens, and S. Massar, *Opt. Express* **22**, 3089 (2014).
8. B. Kuyken, X. Liu, R. M. Osgood, Jr., R. Baets, G. Roelkens, and W. Green, *Opt. Express* **19**, 20172 (2011).
9. H. Yokoyama, H. Tsubokawa, H. Guo, J.-I. Shikata, K.-I. Sato, K. Takashima, K. Kashiwagi, N. Saito, H. Taniguchi, and H. Ito, *J. Biomed. Opt.* **12**, 054019 (2007).
10. Q. Xu, K. Shi, and Z. Liu, *J. Raman Spectrosc.* **42**, 2100 (2011).
11. H. Mikami, M. Shiozawa, M. Shirai, and K. Watanabe, *Opt. Express* **23**, 2872 (2015).
12. L. Zhang, Y. Yan, Y. Yue, Q. Lin, O. Painter, R. G. Beausoleil, and A. E. Willner, *Opt. Express* **19**, 11584 (2011).

13. R. Halir, Y. Okawachi, J. S. Levy, M. A. Foster, M. Lipson, and A. L. Gaeta, *Opt. Lett.* **37**, 1685 (2012).
14. S. Miller, K. Luke, Y. Okawachi, J. Cardenas, A. L. Gaeta, and M. Lipson, *Opt. Express* **22**, 26517 (2014).
15. F. Leo, U. Dave, S. Keyvaninia, B. Kuyken, and G. Roelkens, *Opt. Lett.* **39**, 711 (2014).
16. L. Yin, Q. Lin, and G. P. Agrawal, *Opt. Lett.* **32**, 391 (2007).
17. A. Subramanian, P. Neutens, A. Dhakal, R. Jansen, T. Claes, X. Rottenberg, F. Peyskens, S. Selvaraja, P. Helin, B. Dubois, K. Leysens, S. Severi, P. Deshpande, R. Baets, and P. Van Dorpe, *Photon. J. IEEE* **5**, 2202809 (2013).
18. K. Ikeda, R. E. Saperstein, N. Alic, and Y. Fainman, *Opt. Express* **16**, 12987 (2008).
19. A. Dhakal, A. Z. Subramanian, P. Wuytens, F. Peyskens, N. L. Thomas, and R. Baets, *Opt. Lett.* **39**, 4025 (2014).
20. A. Dhakal, P. Wuytens, F. Peyskens, A. Z. Subramanian, N. Le Thomas, and R. Baets, *Proc. SPIE* **9141**, 91411C (2014).